Hindawi
Advances in Materials Science and Engineering
Volume 2022, Article ID 3489390, 13 pages
https://doi.org/10.1155/2022/3489390

Research Article

Wind-Induced Response Analysis for a Fatigue-Prone Asymmetric Steel Arch Bridge with Inclined Arch Ribs

You-Hua Su, Yan-Ru Wu, and Qing Sun

Department of Civil Engineering, Xi'an Jiaotong University, Xi'an 710049, China

Correspondence should be addressed to Qing Sun; sunq@mail.xjtu.edu.cn

Received 11 June 2021; Accepted 10 December 2021; Published 24 March 2022

Academic Editor: Alicia E. Ares

Steel arch bridges with inclined arch ribs under strong wind fields are prone to fatigue damage due to the stress concentration at the position of hanger connections. Therefore, it is essential to perform the wind-induced response analysis for specified shape hangers, such as inclined hangers, to determine the stress distribution and corresponding influencing factors. In this study, wind-induced response analysis for a fatigue-prone asymmetric steel arch bridge with inclined arch ribs is performed by the numerical simulation approach. The investigated bridge hangers' models are established by using the COMSOL Multiphysics software. The wind-induced stress of the bridge hangers under different wind directions is obtained based on the finite element method. The influential factor of the stress distribution of the bridge hangers on both the windward side and the leeward side is discussed. In addition, the stress peaks of the long hanger and short hanger are achieved for further fatigue analysis. This paper provides a reference for determining the critical fatigue-prone position of an asymmetric steel arch bridge with inclined arch ribs.

1. Introduction

The long-span steel bridges under the conditions of heavy traffic and harsh environment are vulnerable to fatigue damage and failure [1–3]. The wind resistance performance of long-span bridge structures under the cyclic action of wind has become a major concern during the periods of design, construction, and operation [4–6]. Especially, stress concentration generated by long-term cyclic wind loading may cause fatigue damage to long-span arch bridges with hangers. For specified shape hangers, such as inclined hangers, it is essential to perform the wind-induced response analysis to determine the stress distribution and corresponding influence factor including the wind speed and wind direction.

Many research efforts have been devoted to the influence of the wind speed and wind direction variability on civil structures [7–9]. Generally, the wind speed directly determines the size of the wind load [10]. Wang et al. [11] used the improved multirate fusion method to correct the monitoring data for accurate modeling of the wind speed. Zhang et al. [12] presented a quantitative analysis of the wind-induced postcritical performance of bridge decks to highlight the underlying wind-resistant capacity after critical wind speeds. Hu et al. [13] investigated the wind characteristics as well as the flutter performance of a long-span suspension bridge located in a deep-cutting gorge terrain. Especially, the mean wind speed, turbulence intensity, wind angle of attack, wind speed power spectral density, and wind speed coherence varying along the bridge girder were measured and analyzed.

In addition, the wind direction determines the change of wind field environment [14]. Zhang et al. [15] studied the influence effect of the wind direction on the wind field characteristic parameters, and the results show that the wind field characteristic parameters vary greatly among directions. Ye et al. [16] pointed out that the probabilistic modeling of the wind speed and direction can effectively characterize the stochastic properties of the wind field and then presented an extended parameters estimation algorithm for modeling the joint distribution of the wind speed and direction by von Mises distribution based on the Rebmix algorithm. Bao et al. [17] proposed a novel framework for analyzing the dynamic responses of suspended monorail vehicles running over curved bridges under cross winds. The

results show that the wind direction has a great effect on the lateral dynamic response of curved bridges, the lateral force of the guiding tire, and the vertical force of the running tire.

Obviously, the wind speed and direction have a significant impact on the structural dynamic response. However, it is difficult to calculate the stress response of the structure when the wind speed and direction are known by the analytical methods [18–21]. Nowadays, there are a lot of models, such as standard k-ε, realizable k-ε, standard k-ω, and shear-stress-transport (SST) k-ω, to describe the turbulence in computational fluid dynamics (CFD) numerical simulation [22]. Shimada et al. [23] examined the standard k-ε model for various types of aerodynamic instability by comparison with experiments and then discussed the applicability of an unsteady two-dimensional k-ε model to the prediction of these instabilities based on the experimental results. Haque et al. [24] carried out the numerical calculations for the airflow by solving the Reynolds-averaged Navier–Stokes equations coupled with the realizable k-ε turbulence model equation. Sun et al. [25] concerned with the question of an appropriate turbulence model for the computational modeling of bridge deck aeroelasticity, and the result showed that the two-equation standard k-ω turbulence model strikes the right balance between computational efficiency and accuracy in simulating the flow regime. Xu et al. [26] used the k-ω SST model as the turbulence closure for the equations to capture the turbulence effects in the bridge deck-wave interaction. Furthermore, in order to directly identify indicial responses on a bridge, the dynamic nonlinear response of the bridge should be simultaneously considered in CFD, that is, fluid-structure coupling, which considers a motionless solid region immersed in the fluid domain [27]. Glück et al. [28] presented a partitioned coupling approach for fluid-structure interactions and then applied to structures with large displacements. Santo et al. [29] used transient fluid-structure interaction simulations to analyze the dynamic load and stress of structures. Wu et al. [30] simulated one-way fluid-solid coupling interaction based on the fluid flow and static structural modules of the ANSYS finite element software. Thus, these turbulence models are used to calculate the wind field, and the dynamic response model is used to calculate the stress based on the one-way fluid-solid coupling method in this study.

In this paper, the main contributions of this work are as follows: (1) the investigated bridge hangers' models are established by using the COMSOL Multiphysics software, which can calculate one-way fluid-solid coupling and (2) the influence of the wind direction for the bridge hangers is investigated by case studies. The stress distribution of the investigated bridge hangers' stress is obtained based on the dynamic response model. The rest of the paper is organized as follows. In Section 2, the turbulence model, that is, standard k-ε, and the dynamic response model of computational solid mechanics (CSM) are described. In Section 3, the results of the influence of the wind direction are introduced. Finally, Section 4 ends with some conclusions drawn from this study.

2. Methodology

2.1. Computational Fluid Dynamics. Wind load is one of the key parameters in the design of long-span bridges because of its relative low stiffness and damping. The wind tunnel test is usually used to analyze the dynamic characteristics of long-span bridges under wind excitation. In the past two decades, CFD has received increasing attention due to its widespread application in the bridge design as a low-cost complement and supplement to the wind tunnel test. In general, fluids are considered incompressible in the case of aerodynamic loads induced by the wind on long-span bridges. The continuity equation and momentum equation for incompressible fluid can be written as [31]

$$\begin{aligned} \frac{\partial U_i}{\partial x_i} &= 0, \\ U_j \frac{\partial U_i}{\partial x_j} &= \frac{1}{\rho}\frac{\partial}{\partial x_j}\left(-P\delta_{ij} + 2\upsilon S_{ij} + \tau_{ij}\right), \end{aligned} \tag{1}$$

where ρ is the density of air, υ is the kinematic viscosity, P is the pressure, S_{ij} is the velocity strain rate tensor, $S_{ij} = 1/2\,(\partial U_i/\partial x_j + \partial U_j/\partial x_i)$, δ_{ij} is the Kronecker delta, U_i is the mean velocity components, and τ_{ij} is the Reynolds stress terms, which represents the diffusive transport of the momentum by turbulent motion.

The turbulent Reynolds stresses and mean velocity gradients were related by turbulent viscosity based on the Boussinesq approximation, which can be expressed by [31]

$$\tau_{ij} = \upsilon_t\left(\frac{\partial U_i}{\partial x_j} + \frac{\partial U_j}{\partial x_i}\right) - \frac{2}{3}k\delta_{ij}, \tag{2}$$

where k is the turbulent kinetic energy.

If the flow field has a vortex or the number of Reynolds exceeds a certain critical value or the fluid has irregular movement, that is, turbulent flow phenomenon, then it can be solved by turbulence models such as standard k-ε model. For the standard k-ε model, the transport equation of k can be expressed by [32]

$$\begin{aligned} \upsilon_t &= C_\mu \frac{k^2}{\varepsilon}, \\ \frac{\partial \rho k}{\partial t} + \frac{\partial \rho k U_i}{\partial x_i} &= \frac{\partial}{\partial x_j}\left[\left(\upsilon + \frac{\upsilon_t}{\sigma_k}\right)\frac{\partial k}{\partial x_j}\right] + P_k - \rho\varepsilon. \end{aligned} \tag{3}$$

The transport equation for ε can be expressed by [32, 33]

$$\frac{\partial \rho\varepsilon}{\partial t} + \frac{\partial \rho\varepsilon U_i}{\partial x_i} = \frac{\partial}{\partial x_j}\left[\left(\upsilon + \frac{\upsilon_t}{\sigma_\varepsilon}\right)\frac{\partial \varepsilon}{\partial x_j}\right] + \frac{\varepsilon}{k}\left(C_1 P_k - C_2\rho\varepsilon\right), \tag{4}$$

where P_k is the production of turbulent kinetic energy, $P_k = \upsilon_t S^2$, $S = \sqrt{2S_{ij}S_{ij}}$, and other constants are $C_\mu = 0.09$, $\sigma_\varepsilon = 1.3$, $\sigma_k = 1.0$, $C_1 = 1.44$, and $C_2 = 1.92$.

2.2. Computational Solid Mechanics. The wind pressure acting on the surface of the bridge is equivalent to the concentrated force and concentrated moment acting on the center of mass of the bridge. The dynamic equations can be established by the D'Alembert theory, which can be expressed by [34]

$$M\ddot{X} + C\dot{X} + KX = F, \tag{5}$$

where M is the mass matrix, C is the damping matrix representing the inner or structural damping of the structure, K is the stiffness matrix, F characterizes the load acting on the structure caused by the fluid, X is the displacement, $\dot{X}$ is the velocity, and $\ddot{X}$ is the acceleration.

In light of the displacement-based finite element method, which is a systematic procedure for approximating continuous functions as discrete models, the stress and strain can be solved by [35]

$$\begin{aligned} \varepsilon_{ij} &= \frac{1}{2}\left(X_{ij} + X_{ji}\right)(i, j = 1, 2, 3), \\ \sigma_{ij} &= \lambda\varepsilon_{kk}\delta_{ij} + 2\mu\varepsilon_{ij}\,(i, j, k = 1, 2, 3), \\ \lambda &= \frac{E\nu}{(1+\nu)(1-2\nu)}, \\ \mu &= \frac{E}{2(1+\nu)}, \end{aligned} \tag{6}$$

where σ_{ij} is the stress, ε_{ij} is the strain, E is the elasticity modulus, and ν is Poisson's ratio.

3. Calculation and Analysis

COMSOL Multiphysics is a finite element software for analysis of CFD, solid mechanics, one-way fluid-solid coupling, etc. [36, 37]. An asymmetric steel arch bridge with inclined arch ribs in [38] is selected to carry out wind-induced stress response analysis, as shown in Figure 1. The simplified model of bridge hangers is divided based on the COMSOL software, as shown in Figure 2. In the bridge hanger model, there is a circular cross-sectional area of 0.0017 m^2 for interior hangers and 0.00042 m^2 for exterior hangers. Young's modulus is 2.06×10^5 MPa, and Poisson's ratio is 0.3. The top and bottom of the bridge hangers are fixed. In this case study, the wind speed is set as 20 m/s. 7 case studies in this paper are carried out to obtain the distributions of the bridge hanger's wind field and stress field for different wind directions and different turbulence models.

In Case 1, the wind field changes of bridge hangers at different heights under the wind direction angle of 0°/180° are calculated based on the COMSOL finite element software, as shown in Figure 3. Obviously, the maximum and minimum wind speeds are not the same at different heights of bridge hangers. Specifically, when the height z is 10 m, the maximum wind speed is 20.8 m/s and the minimum wind speed is 15.3 m/s. When the height z is 5 m, the maximum wind speed is 21.0 m/s and the minimum wind speed is 14.0 m/s. When the height z is 3 m, the maximum wind speed is 21.1 m/s and the minimum wind speed is 9.3 m/s. When the height z is 1.0 m, the maximum wind speed is 21.1 m/s and the minimum wind speed is 6.39 m/s. It can be seen from Figure 3 that the wind field varies with heights under the same wind speed.

Furthermore, the von Mises stress change of the bridge hanger under the wind field is calculated based on the structural dynamic model. Especially, the fixed end of the top of the bridge hanger is selected as the reference point, and the von Mises stress changes between different hangers are compared, as shown in Figure 4. It can be found that the greater stress is observed at the fixed end of the longer hanger. Specifically, the maximum von Mises stress of the long hanger is 12.321 MPa and the minimum von Mises stress is 0.017 MPa. The maximum von Mises stress of the short hanger is 0.813 MPa and the minimum von Mises stress is 0.001 MPa.

For case study 2, the wind field changes of bridge hangers at different heights under the wind direction angle 30°/150° are calculated, as shown in Figure 5. As can be seen from Figure 5, the maximum and minimum wind speeds are also different at different heights. Specifically, when the height z is 10 m, the maximum wind speed is 20.5 m/s and the minimum wind speed is 17.2 m/s; when the height z is 5 m, the maximum wind speed is 20.7 m/s and the minimum wind speed is 16 m/s; when the height z is 3 m, the maximum wind speed is 20.8 m/s and the minimum wind speed is 15.9 m/s; and when the height z is 1 m, the maximum wind speed is 20.7 m/s and the minimum wind speed is 15.1 m/s.

Especially, the fixed end of the top hanger is selected as the reference point and the von Mises stress changes between different hangers are compared, which can be seen in Figure 6. The maximum von Mises stress of the long hanger is 8.187 MPa and the minimum is 0.136 MPa; the maximum von Mises stress of the short hanger is 0.931 MPa and the minimum is 0.003 MPa.

For case study 3 (the wind direction angle is 60°/120°), as can be seen from Figure 7, when the height z is 10 m, the maximum wind speed is 20.4 m/s and the minimum wind speed is 16.8 m/s; when the height z is 5 m, the maximum wind speed is 20.5 m/s and the minimum wind speed is 15.9 m/s; when the height z is 3 m, the maximum wind speed is 20.4 m/s and the minimum wind speed is 15.1 m/s; when the height z is 1 m, the maximum wind speed is 20.4 m/s and the minimum wind speed is 14.6 m/s.

Likewise, the fixed end of the top of the bridge hanger is selected as the reference point. The maximum von Mises stress of the long hanger is 7.768 MPa and the minimum von Mises stress is 0.088 MPa; the maximum von Mises stress of the short hanger is 1.144 MPa and the minimum von Mises stress is 0.018 MPa, as shown in Figure 8.

The wind field changes of bridge hangers at different heights under the wind direction angle 90° are calculated as case study 4. As can be seen from Figure 9, when the height z is 10 m, the maximum wind speed is 20.5 m/s and the minimum wind speed is 11.9 m/s; when the height z is 5 m, the maximum wind speed is 20.5 m/s and the minimum wind speed is 13.3 m/s; when the height z is 3 m, the maximum wind speed is 20.6 m/s and the minimum wind speed is 13.9 m/s; and when the height z is 1 m, the maximum wind speed is 20.5 m/s and the minimum wind speed is 13.5 m/s.

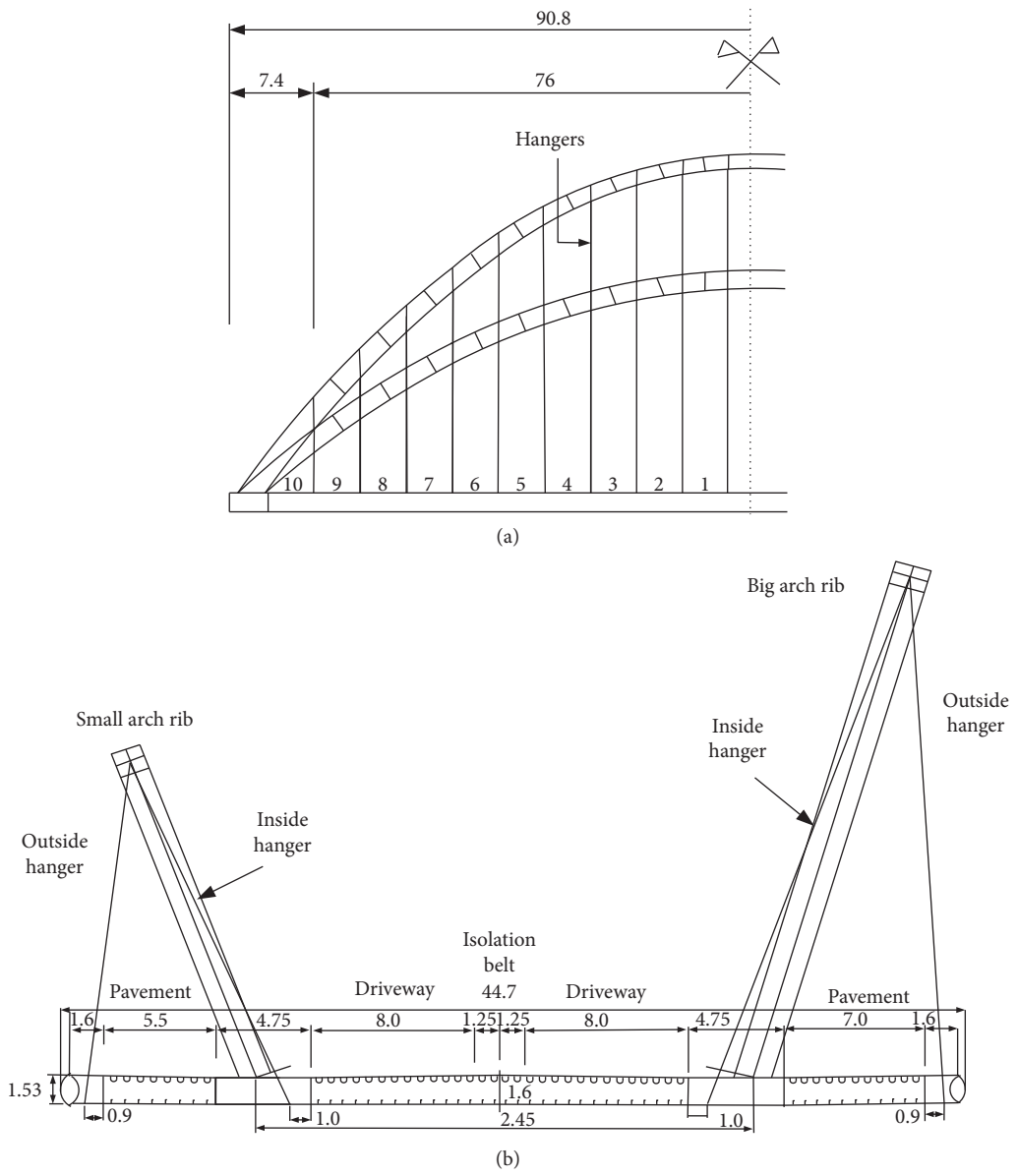

Figure 1: Details of the investigated bridge [38]. (a) Elevation. (b) Deck cross section at the center span.

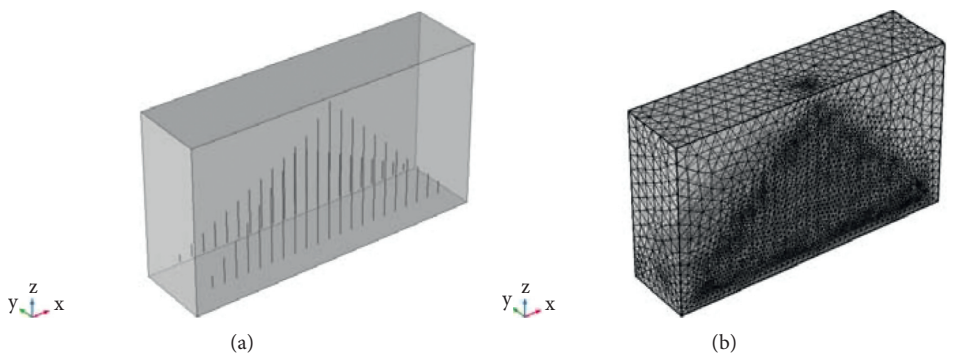

Figure 2: Finite element model. (a) Wind field simulation. (b) Calculation mesh.

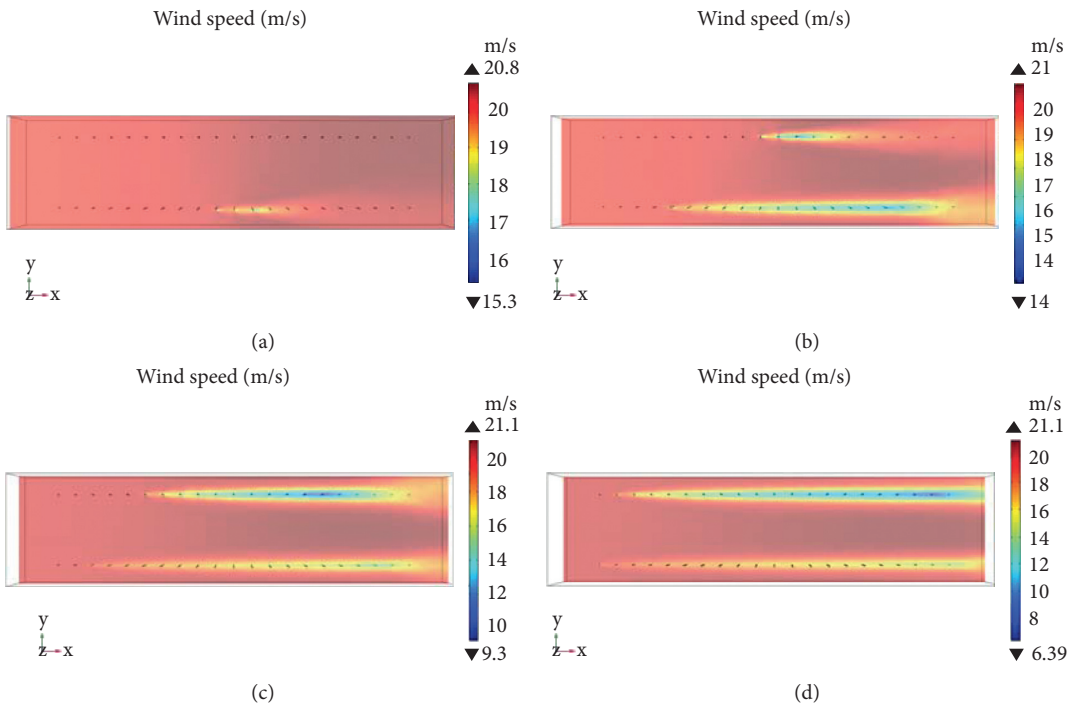

Figure 3: Influence of height for wind field (wind direction = 0°/180°). (a) 0°/180°, $z = 10$ m. (b) 0°/180°, $z = 5$ m. (c) 0°/180°, $z = 3$ m. (d) 0°/180°, $z = 1$ m.

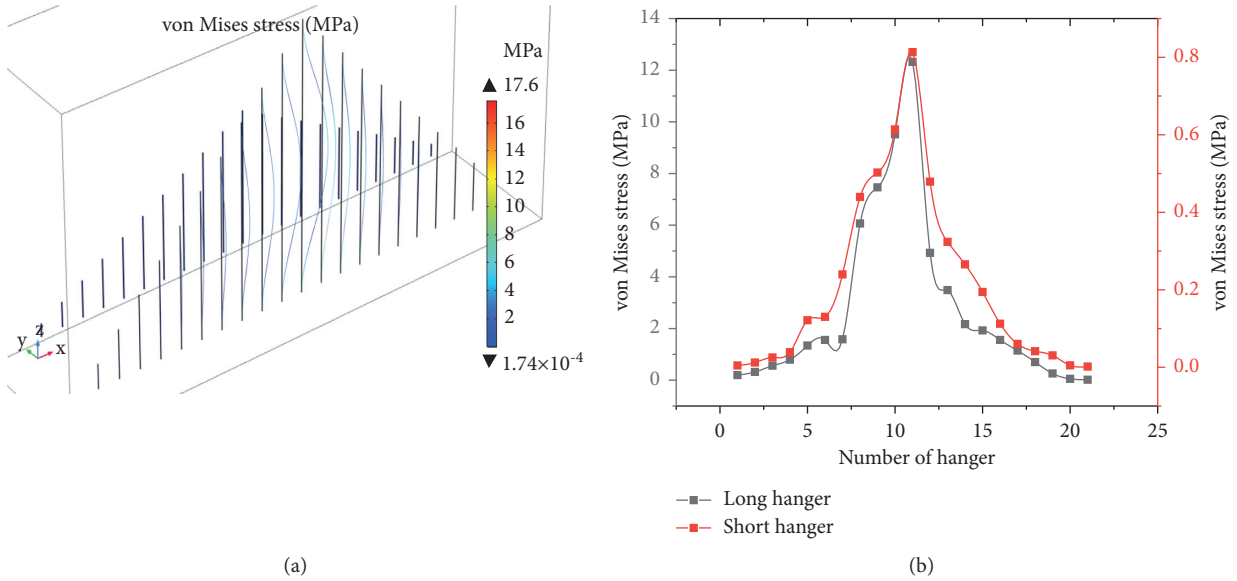

Figure 4: Stress distribution of hangers (wind direction = 0°/180°).

As can be seen from Figure 10, the maximum von Mises stress of the long hanger is 15.844 MPa and the minimum von Mises stress is 0.091 MPa; and the maximum von Mises stress of the short hanger is 1.319 MPa and the minimum von Mises stress is 0.016 MPa.

For case 5 (the wind direction angle is 210°/330°), as can be seen from Figure 11, when the height z is 10 m, the maximum wind speed is 20.5 m/s and the minimum wind speed is 16.8 m/s; when the height z is 5 m, the maximum wind speed is 20.5 m/s and the minimum wind speed is 16.1 m/s; when the height z is 3 m, the maximum wind speed is 20.5 m/s and the minimum wind speed is 15.2 m/s; and when the height z is 1 m, the maximum wind speed is 20.6 m/s and the minimum wind speed is 14.6 m/s.

The maximum von Mises stress of the long hanger is 8.263 MPa and the minimum von Mises stress is 0.084 MPa;

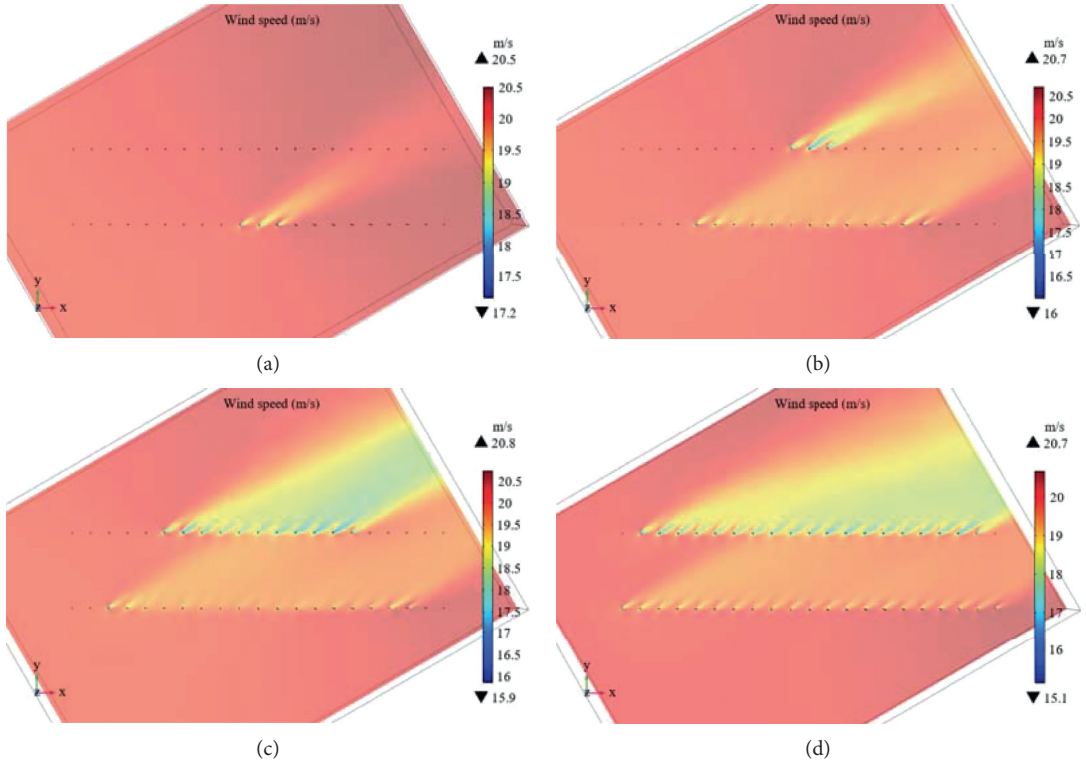

FIGURE 5: Influence of height for wind field (wind direction = 30°/120°). (a) 30°/150°, $z = 10$ m. (b) 30°/150°, $z = 5$ m. (c) 30°/150°, $z = 3$ m. (d) 30°/150°, $z = 1$ m.

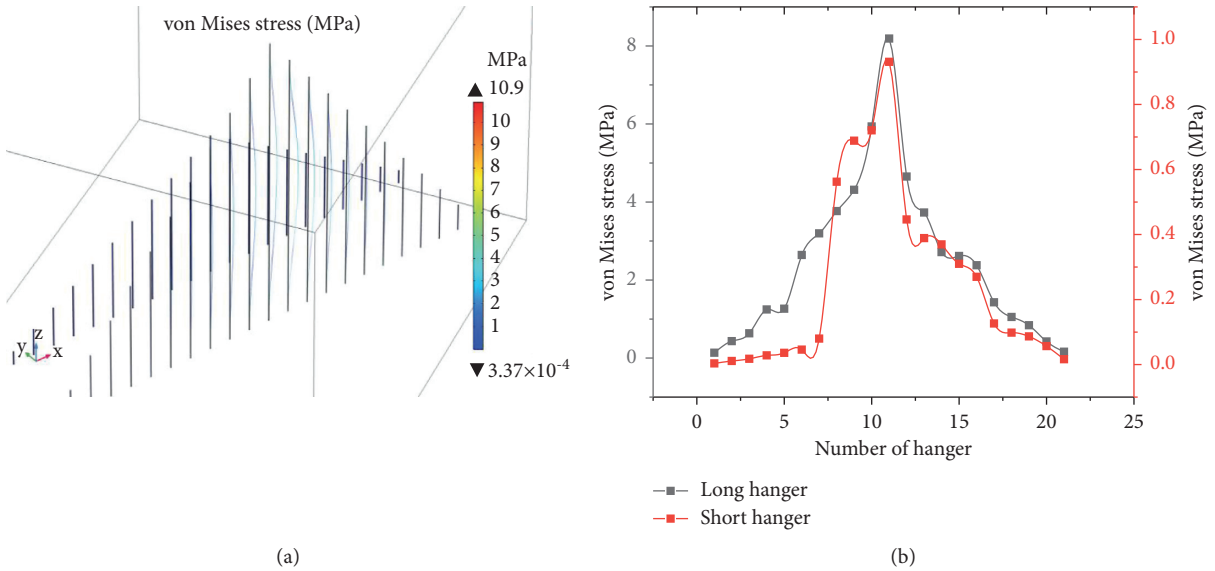

FIGURE 6: Stress distribution of hangers (wind direction = 30°/150°).

the maximum von Mises stress of the short hanger is 1.156 MPa and the minimum von Mises stress is 0.016 MPa, as shown in Figure 12.

For case 6 (the wind direction angle is 240°/300°), as can be seen from Figure 13, when the height z is 10 m, the maximum wind speed is 20.6 m/s and the minimum wind speed is 16.7 m/s; when the height z is 5 m, the maximum wind speed is 20.5 m/s and the minimum wind speed is 16 m/s; when the height z is 3 m, the maximum wind speed is 20.6 m/s and the minimum wind speed is 15.2 m/s; and when the height z is 1 m, the maximum wind speed is 20.7 m/s and the minimum wind speed is 13.6 m/s.

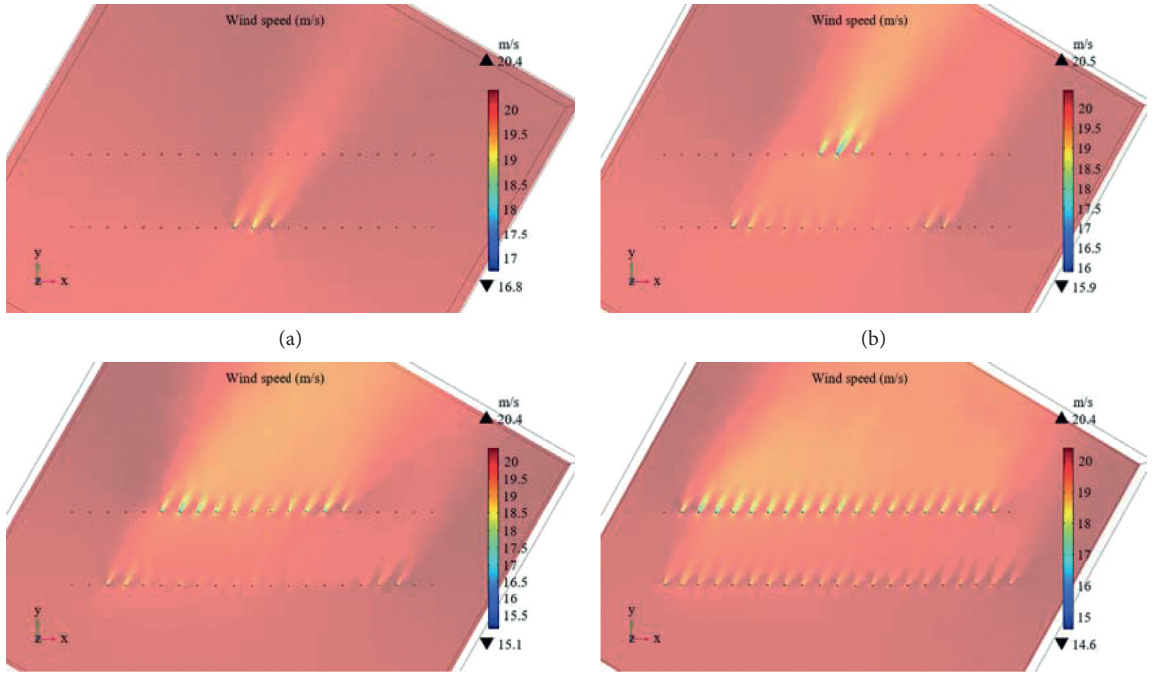

FIGURE 7: Influence of height for wind field (wind direction = 60°/120°). (a) 60°/120°, $z = 10$ m. (b) 60°/120°, $z = 5$ m. (c) 60°/120°, $z = 3$ m. (d) 60°/120°, $z = 1$ m.

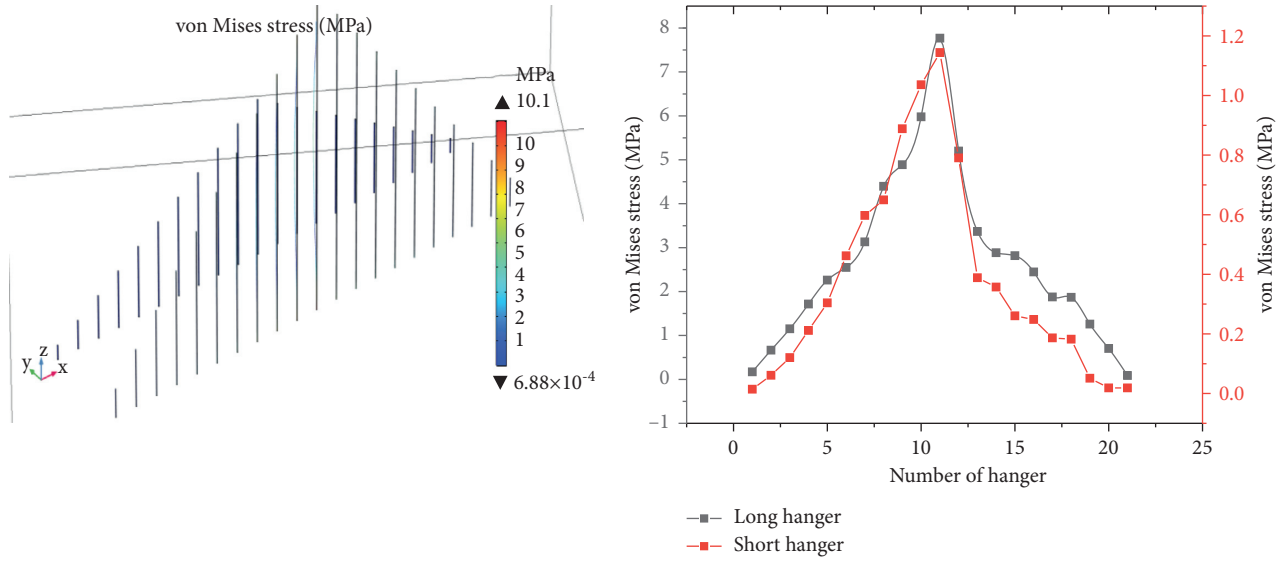

FIGURE 8: Stress distribution of hangers (wind direction = 60°/120°).

The maximum von Mises stress of the long hanger is 7.073 MPa and the minimum von Mises stress is 0.213 MPa; and the maximum von Mises stress of the short hanger is 1.358 MPa and the minimum von Mises stress is 0.007 MPa, as shown in Figure 14.

For case study 7 (the wind direction angle is 270°), as can be seen from Figure 15, when the height z is 10 m, the maximum wind speed is 20.5 m/s and the minimum wind speed is 14.9 m/s; when the height z is 5 m, the maximum wind speed is 20.8 m/s and the minimum wind speed is 13.6 m/s; when the height z is 3 m, the maximum wind speed is 21 m/s and the minimum wind speed is 12.1 m/s; and when the height z is 1 m, the maximum wind speed is 21 m/s and the minimum wind speed is 13.7 m/s.

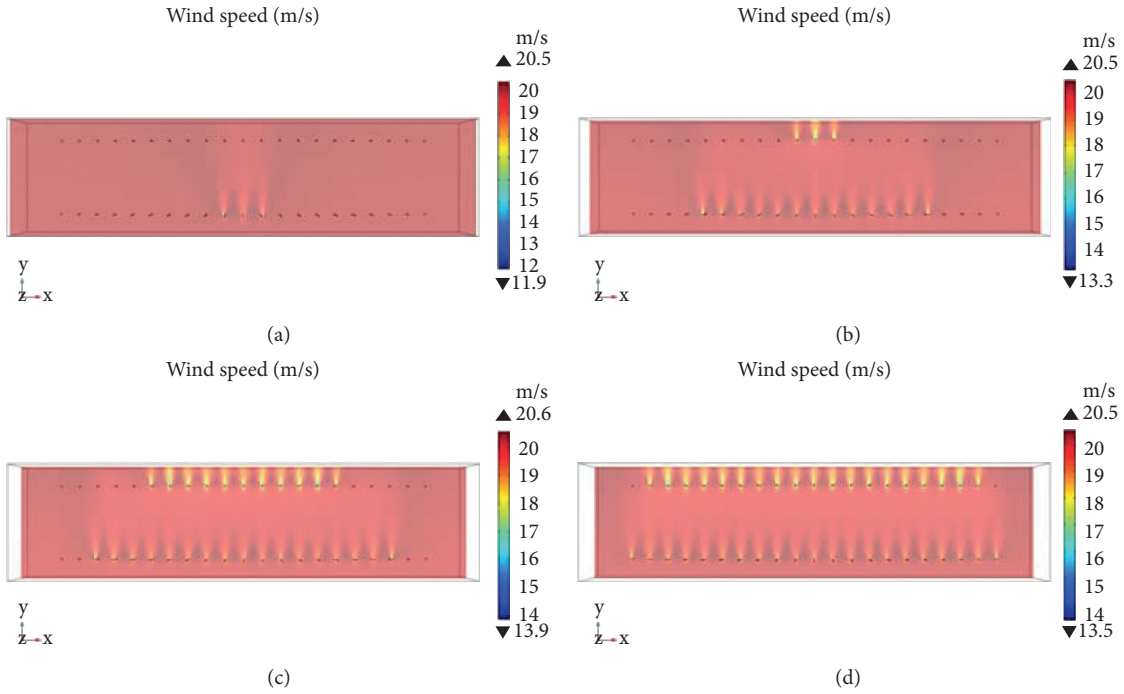

Figure 9: Influence of height for wind field (wind direction = 90°). (a) 90°, $z = 10$ m. (b) 90°, $z = 5$ m. (c) 90°, $z = 3$ m. (d) 90°, $z = 1$ m.

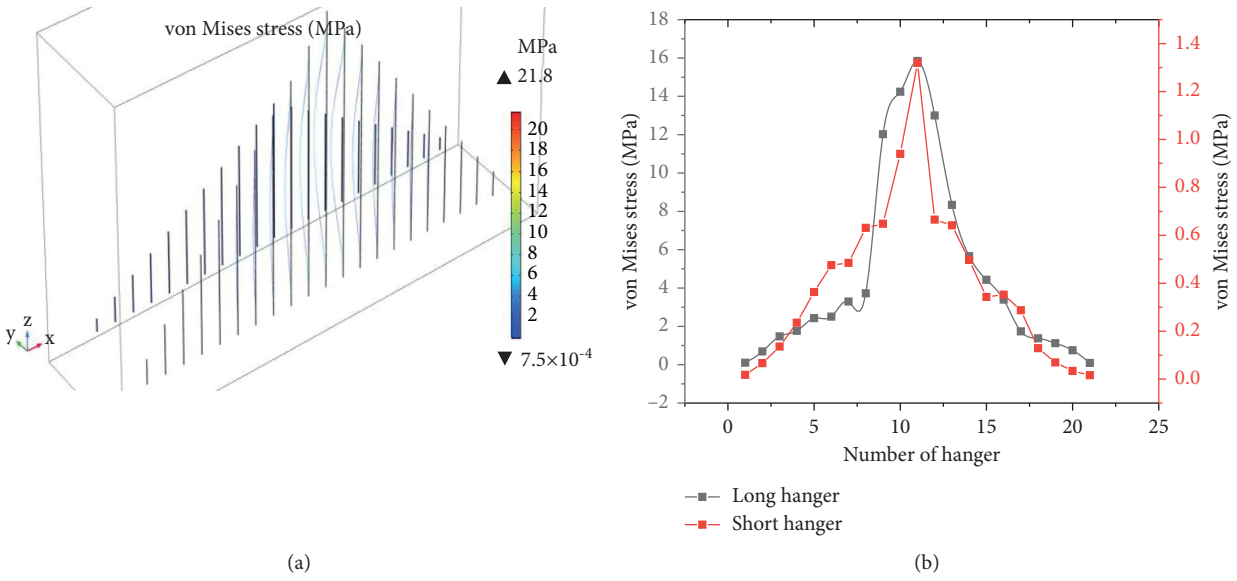

Figure 10: Stress distribution of hangers (wind direction = 90°).

The maximum von Mises stress of the long hanger is 15.967 MPa and the minimum von Mises stress is 0.239 MPa; and the maximum von Mises stress of the short hanger is 1.83 MPa and the minimum von Mises stress is 0.035 MPa, as shown in Figure 16.

It can be seen from case studies 1–7, the maximum and minimum wind speeds are not the same at different heights. The greater stress is observed at the fixed end of the longer hanger when the fixed end of the top of the bridge hanger is selected as the reference point. Case studies 1–7 follow the

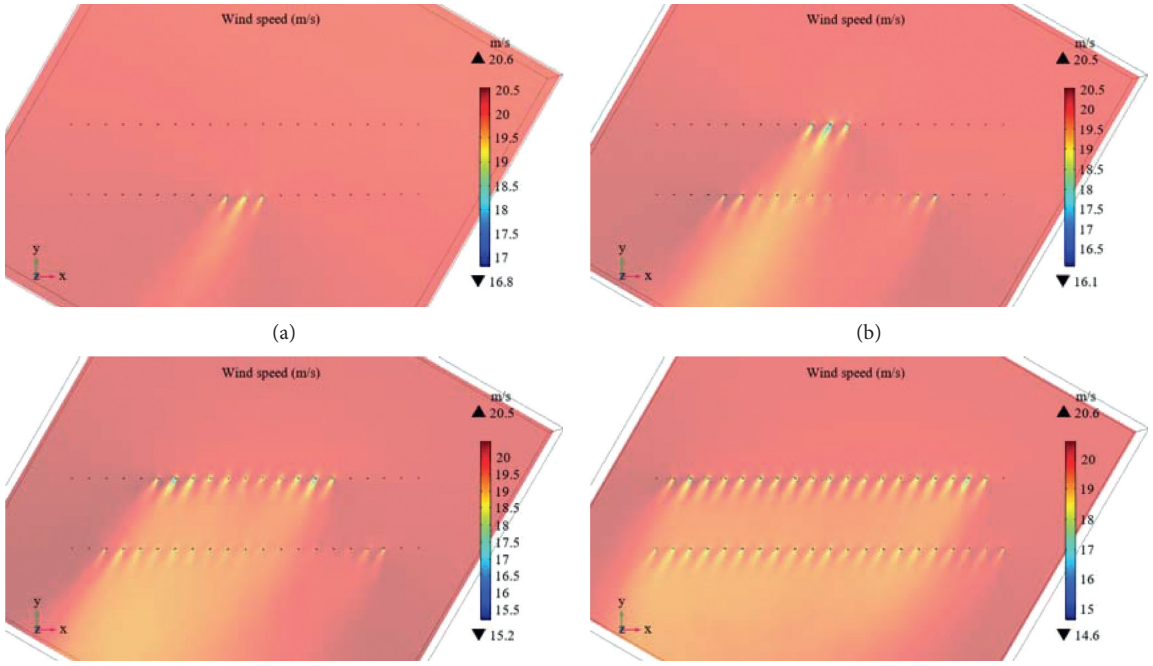

FIGURE 11: Influence of height for wind field (wind direction = 210°/330°). (a) 210°/330°, $z = 10$ m. (b) 210°/330°, $z = 5$ m. (c) 210°/330°, $z = 3$ m. (d) 210°/330°, $z = 1$ m.

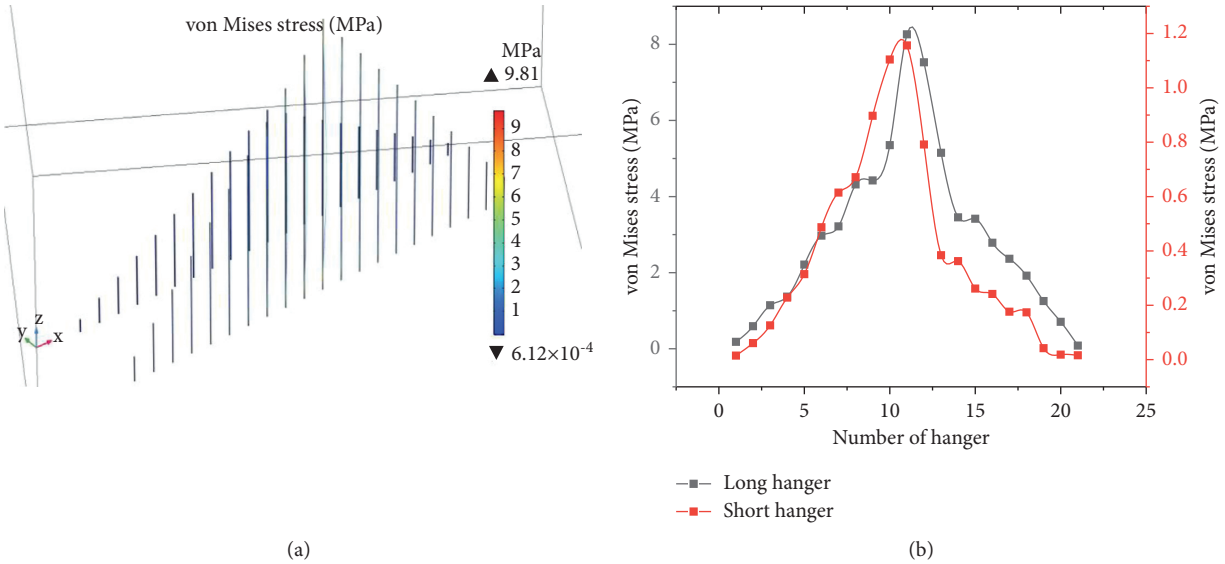

FIGURE 12: Stress distribution of hangers (wind direction = 210°/330°).

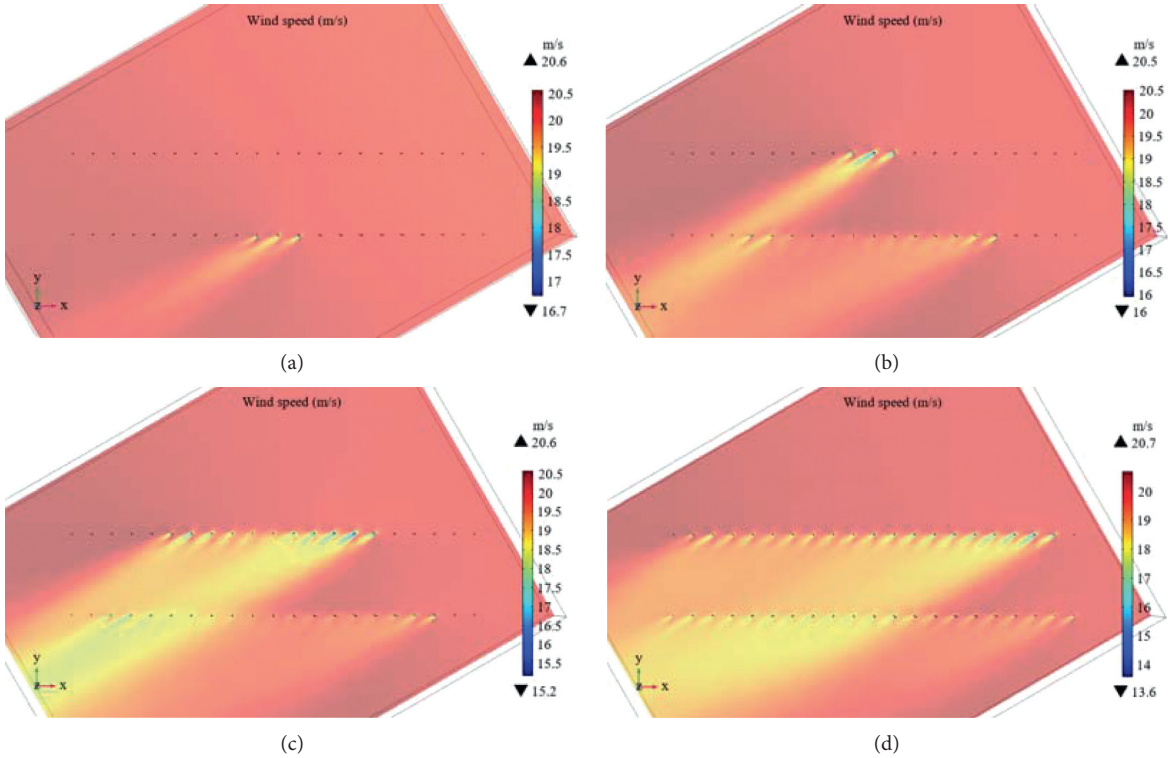

Figure 13: Influence of height for wind field (wind direction = 240°/300°). (a) 240°/300°, $z = 10$ m. (b) 240°/300°, $z = 5$ m. (c) 240°/300°, $z = 3$ m. (d) 240°/300°, $z = 1$ m.

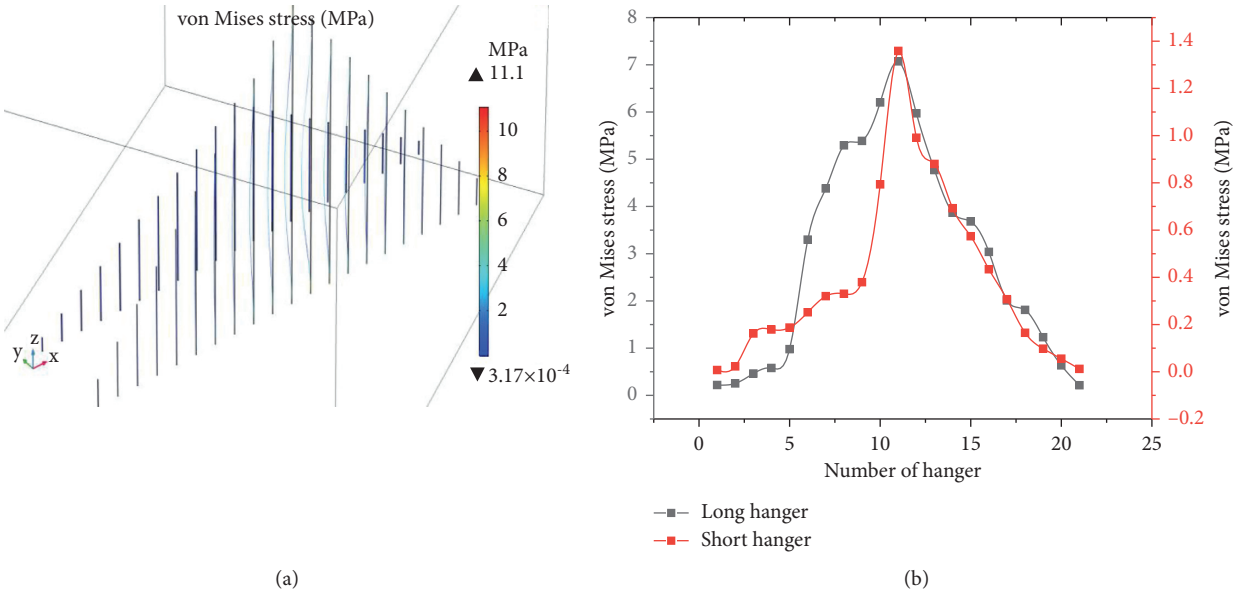

Figure 14: Stress distribution of hangers (wind direction = 240°/300°).

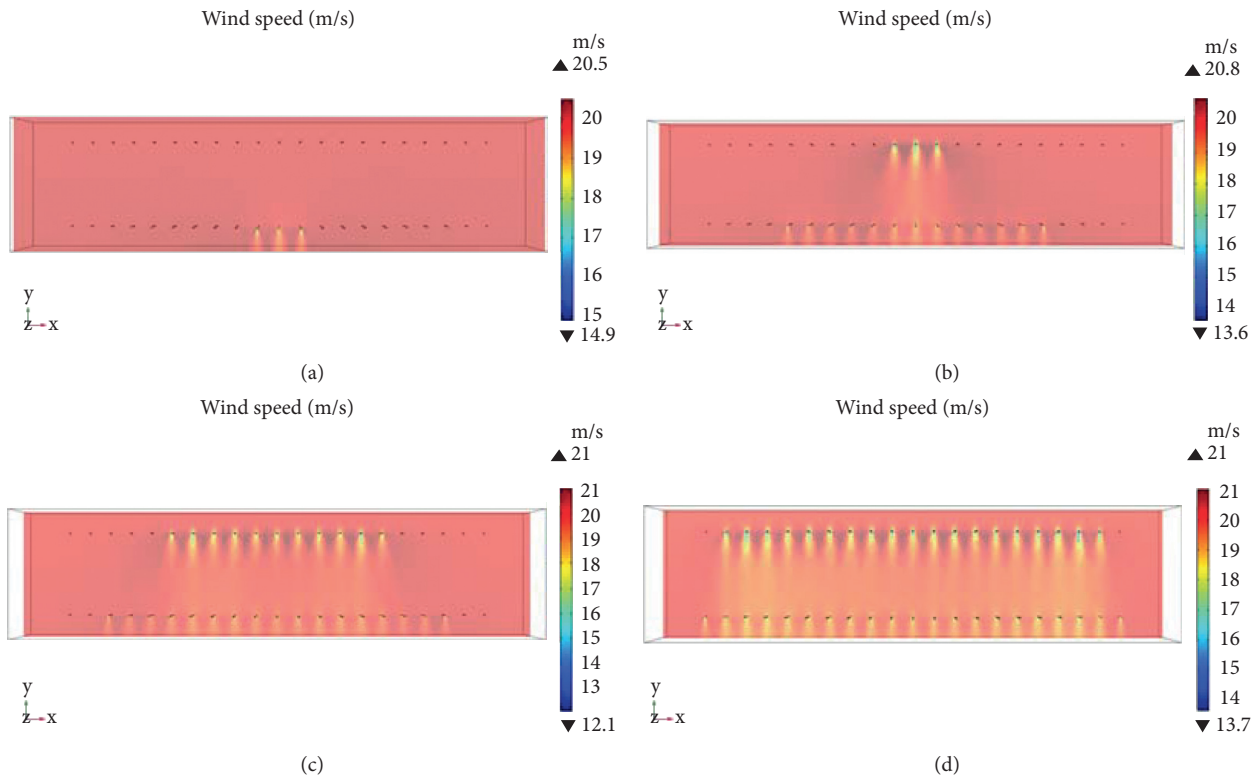

FIGURE 15: Influence of height for wind field (wind direction = 270°). (a) 270°, $z = 10$ m. (b) 270°, $z = 5$ m. (c) 270°, $z = 3$ m. (d) 270°, $z = 1$ m.

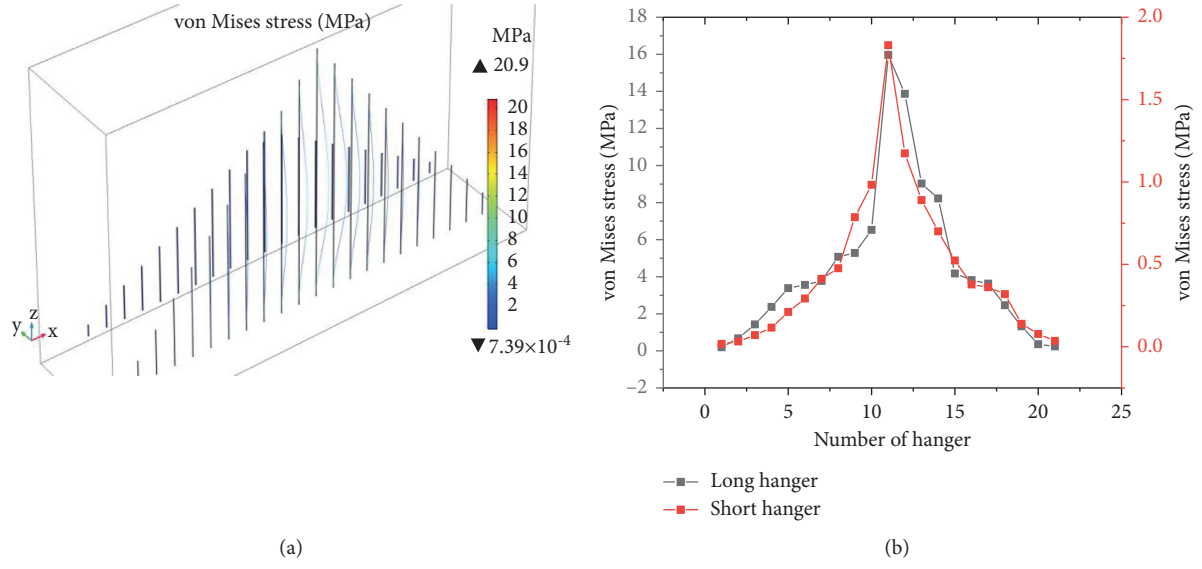

FIGURE 16: Stress distribution of hangers (wind direction = 270°).

same laws for determining the critical fatigue-prone position of the asymmetric steel arch bridge with inclined arch ribs.

4. Conclusions

In this study, a numerical simulation approach is performed to analyze the wind response of a fatigue-prone asymmetric steel arch bridge with inclined arch ribs. The model of the bridge hanger investigated is established by using the COMSOL Multiphysics software. The bridge hangers with different wind directions are obtained based on the finite element method considering the influencing factors of the stress distribution of both windward and leeward bridge hangers. In addition, the stress peaks of long and short hangers are checked for further analysis. The influence of the wind direction for the wind field of bridge hangers are

investigated by using seven cases, and the von Mises stress of bridge hangers is calculated based on fluid-solid coupling. The main conclusions drawn from this study are summarized as follows:

(1) The maximum stress of the hangers is observed at the top of the long hanger under different wind directions. That is, the critical fatigue-prone position of the asymmetric steel arch bridge with inclined arch ribs is at the top of the long hanger.

(2) The stress of the bridge hangers on the windward side is greater than that on the leeward side; it is necessary to pay close attention to the fatigue analysis of long hangers on the windward side.

Data Availability

The data used to support the findings of this study are included within the article.

Ethical Approval

Ethical review and approval were waived for this study because the institutions of the authors who participated in data collection do not require IRB review and approval.

Conflicts of Interest

The authors declare no conflicts of interest.

Authors' Contributions

Y. S. provided acquisition of funding, conducted the investigation, and designed the study methodology. Y. W. performed the software analysis. Q. S. supervised the research work. Y. S., Y. W., and Q. S. wrote, reviewed, and edited the manuscript. All authors have read and agreed to the published version of the manuscript.

Acknowledgments

The work described in this paper was supported by the Shaanxi Provincial Natural Science Foundation of China (Grant no. 2021JQ-035).

References

[1] X. W. Ye, P. S. Xi, and Y. H. Su, "Analysis of non-stationary wind characteristics at an arch bridge using structural health monitoring data," *Journal of Civil Structural Health Monitoring*, vol. 7, no. 4, pp. 573–587, 2017.

[2] X. W. Ye, Y. H. Su, T. Jin, B. Chen, and J. P. Han, "Master S-N curve-based fatigue life assessment of steel bridges using finite element model and field monitoring data," *International Journal of Structural Stability and Dynamics*, vol. 19, no. 1, Article ID 1940013, 2019.

[3] Y. H. Su, X. W. Ye, and Y. Ding, "ESS-based probabilistic fatigue life assessment of steel bridges: Methodology, numerical simulation and application," *Engineering Structures*, vol. 253, Article ID 113802, 2022.

[4] Y. Ding, G. Zhou, A. Li, and Y. Deng, "Statistical characteristics of sustained wind environment for a long-span bridge based on long-term field measurement data," *Wind and Structures*, vol. 17, no. 1, pp. 43–68, 2013.

[5] S. Kim, J. Cheung, J. Park, and S. Na, "Image-based back analysis for tension estimation of suspension bridge hanger cables," *Structural Control and Health Monitoring*, vol. 27, no. 4, Article ID e2508, 2020.

[6] X. Xu, X. Zheng, C. Zhou, and X. Chen, "Stress analysis of rigid hanger of railway arch bridge based on vehicle-bridge coupling vibration," *Journal of Vibroengineering*, vol. 22, no. 2, pp. 427–436, 2020.

[7] H. Luo, Z. Li, Q. Xiong, and A. Jiang, "Study on the wind-induced fatigue of heliostat based on the joint distribution of wind speed and direction," *Solar Energy*, vol. 207, no. 4, pp. 668–682, 2020.

[8] H. Arslan, H. Baltaci, B. O. Akkoyunlu, S. Karanfil, and M. Tayanc, "Wind speed variability and wind power potential over Turkey: case studies for Çanakkale and İstanbul," *Renewable Energy*, vol. 145, no. 1, pp. 1020–1032, 2020.

[9] B. Fu, J. Zhao, B. Li et al., "Fatigue reliability analysis of wind turbine tower under random wind load," *Structural Safety*, vol. 87, Article ID 101982, 2020.

[10] G. Santamaría-Bonfil, A. Reyes-Ballesteros, and C. Gershenson, "Wind speed forecasting for wind farms: a method based on support vector regression," *Renewable Energy*, vol. 85, pp. 790–809, 2016.

[11] Y. Wang, D.-H. Yang, and T.-H. Yi, "Accurate correlation modeling between wind speed and bridge girder displacement based on a multi-rate fusion method," *Sensors*, vol. 21, no. 6, Article ID 1967, 2021.

[12] M. Zhang, F. Xu, and Y. Han, "Assessment of wind-induced nonlinear post-critical performance of bridge decks," *Journal of Wind Engineering and Industrial Aerodynamics*, vol. 203, Article ID 104251, 2020.

[13] P. Hu, Y. Han, C. S. Cai, and W. Cheng, "Wind characteristics and flutter performance of a long-span suspension bridge located in a deep-cutting gorge," *Engineering Structures*, vol. 233, no. 1, Article ID 111841, 2021.

[14] M. Rahimpour and P. Oshkai, "The effects of unsteady change in wind direction on the airflow over the helicopter platform of a polar icebreaker," *Ocean Engineering*, vol. 172, no. 1, pp. 22–30, 2019.

[15] J. Zhang, M. Zhang, Y. Li, F. Jiang, L. Wu, and D. Guo, "Comparison of wind characteristics in different directions of deep-cut gorges based on field measurements," *Journal of Wind Engineering and Industrial Aerodynamics*, vol. 212, Article ID 104595, 2021.

[16] X. W. Ye, P. S. Xi, and M. Nagode, "Extension of REBMIX algorithm to von Mises parametric family for modeling joint distribution of wind speed and direction," *Engineering Structures*, vol. 183, pp. 1134–1145, 2019.

[17] Y. Bao, H. Xiang, Y. Li, and G. Hou, "Dynamic effects of turbulent crosswinds on a suspended monorail vehicle-curved bridge coupled system," *Journal of Vibration and Control*, pp. 1–11, 2021.

[18] R. O. Ruiz, L. Loyola, and J. F. Beltran, "Stress cycle assessment of cables under wind-induced vibrations: a general probabilistic approach," *KSCE Journal of Civil Engineering*, vol. 24, no. 1, pp. 153–165, 2020.

[19] Y. Han, K. Li, C. S. Cai, L. Wang, and G. Xu, "Fatigue reliability assessment of long-span steel-truss suspension bridges under the combined action of random traffic and wind loads," *Journal of Bridge Engineering*, vol. 25, no. 3, pp. 04020003.1–04020003.10, 2020.

[20] S.-M. Wang, J.-D. Yau, Y.-F. Duan et al., "Prediction of crosswind-induced derailment of train-rail-bridge system by vector mechanics," *Journal of Engineering Mechanics*, vol. 146, no. 12, Article ID 04020132, 2020.

[21] M. Motaleb, W. Lindquist, A. Ibrahim, and R. Hindi, "Repair assessment for distortion-induced fatigue cracks in a seismically retrofitted double-deck bridge complex," *Engineering Structures*, vol. 183, no. 3, pp. 124–134, 2019.

[22] A. Khalilzadeh, H. Ge, and H. D. Ng, "Effect of turbulence modeling schemes on wind-driven rain deposition on a mid-rise building: CFD modeling and validation," *Journal of Wind Engineering and Industrial Aerodynamics*, vol. 184, pp. 362–377, 2019.

[23] K. Shimada and T. Ishihara, "Predictability of unsteady two-dimensional k-ε model on the aerodynamic instabilities of some rectangular prisms," *Journal of Fluids and Structures*, vol. 28, pp. 20–39, 2012.

[24] S. M. E. Haque, M. G. Rasul, M. M. K. Khan, A. V. Deev, and N. Subaschandar, "Influence of the inlet velocity profiles on the prediction of velocity distribution inside an electrostatic precipitator," *Experimental Thermal and Fluid Science*, vol. 33, no. 2, pp. 322–328, 2009.

[25] D. Sun, J. S. Owen, and N. G. Wright, "Application of the k-ω turbulence model for a wind-induced vibration study of 2D bluff bodies," *Journal of Wind Engineering and Industrial Aerodynamics*, vol. 97, no. 2, pp. 77–87, 2009.

[26] G. Xu and C. S. Cai, "Numerical investigation of the lateral restraining stiffness effect on the bridge deck-wave interaction under Stokes waves," *Engineering Structures*, vol. 130, pp. 112–123, 2017.

[27] S. de Miranda, L. Patruno, F. Ubertini, and G. Vairo, "Indicial functions and flutter derivatives: a generalized approach to the motion-related wind loads," *Journal of Fluids and Structures*, vol. 42, pp. 466–487, 2013.

[28] M. Glück, M. Breuer, F. Durst, A. Halfmann, and E. Rank, "Computation of wind-induced vibrations of flexible shells and membranous structures," *Journal of Fluids and Structures*, vol. 17, no. 5, pp. 739–765, 2003.

[29] G. Santo, M. Peeters, W. Van Paepegem, and J. Degroote, "Dynamic load and stress analysis of a large horizontal axis wind turbine using full scale fluid-structure interaction simulation," *Renewable Energy*, vol. 140, pp. 212–226, 2019.

[30] Y. Wu, L. Qi, H. Zhang, E. M. Musiu, Z. Yang, and P. Wang, "Design of UAV downwash airflow field detection system based on strain effect principle," *Sensors*, vol. 19, no. 11, Article ID 2630, 2019.

[31] Y. Qi and T. Ishihara, "Numerical study of turbulent flow fields around of a row of trees and an isolated building by using modified k-ε model and LES model," *Journal of Wind Engineering and Industrial Aerodynamics*, vol. 177, pp. 293–305, 2018.

[32] K. Nakajima, R. Ooka, and H. Kikumoto, "Evaluation of k-ε Reynolds stress modeling in an idealized urban canyon using LES," *Journal of Wind Engineering and Industrial Aerodynamics*, vol. 175, pp. 213–228, 2018.

[33] M. Lateb, C. Masson, T. Stathopoulos, and C. Bédard, "Comparison of various types of k-ε models for pollutant emissions around a two-building configuration," *Journal of Wind Engineering and Industrial Aerodynamics*, vol. 115, pp. 9–21, 2013.

[34] M. Glück, M. Breuer, F. Durst, A. Halfmann, and E. Rank, "Computation of fluid-structure interaction on lightweight structures," *Journal of Wind Engineering and Industrial Aerodynamics*, vol. 89, no. 14-15, pp. 1351–1368, 2001.

[35] S. Celal and A. E. Tekkaya, *Finite Element Method*, CIRP Encyclopedia of Production Engineering, Berlin, Germany, 2014.

[36] S. Zhou, Y. Ding, Z. Wang et al., "Weathering of roofing insulation materials under multi-field coupling conditions," *Materials*, vol. 12, no. 20, Article ID 3348, 2019.

[37] Y. Ding, T.-L. Yang, H. Liu et al., "Experimental study and simulation calculation of the chloride resistance of concrete under multiple factors," *Applied Sciences*, vol. 11, no. 12, Article ID 5322, 2021.

[38] X. Hu, X. Xie, Z. Tang, Y. Shen, P. Wu, and L. Song, "Case study on stability performance of asymmetric steel arch bridge with inclined arch ribs," *Steel and Composite Structures*, vol. 18, no. 1, pp. 273–288, 2015.